

Influence of shaped boundaries on propagating compaction bands in brittle porous mediaDavid M. Riley , Julio R. Valdes , Itai Einav , and François Guillard *Particles and Grains Laboratory, School of Civil Engineering, The University of Sydney, Sydney, New South Wales 2006, Australia**and Geo-Innovations Research Laboratory, Department of Civil, Construction, and Environmental Engineering, San Diego State University, San Diego, California 92182, USA*

(Received 23 May 2023; accepted 13 October 2023; published 18 December 2023)

The compression of brittle porous media can lead to the propagation of compaction bands. Although such localization phenomena have been observed in different geometries, including cuboidal and axisymmetric uniaxial compression, the role of boundary geometry on compaction features has yet to be explored, despite its relevance in geological conditions and industrial processes. To this end, we investigate the influence of shaped boundaries and inhomogeneous inclusions in a model brittle material made of puffed rice cereal. Using a variety of geometries, we show that compaction bands assume the shape of nearby boundaries, but return to a default planar form a distance away from them. Remarkably, the band aligns parallel to characteristic lines of minor principal stress obtained from a simple linear elastic model. The compelling correlation between the rotation of the principal stress directions and compaction band orientation holds implications for the geological interpretation of localized patterns in rocks and for comprehending the formation of weak planes in pharmaceutical tablets.

DOI: [10.1103/PhysRevE.108.064906](https://doi.org/10.1103/PhysRevE.108.064906)**I. INTRODUCTION**

Brittle porous media exhibit specific phenomena that have significant consequences for the industries and natural settings in which they occur. Therefore, understanding the behavior of such materials is crucial in areas as varied as hydrocarbon extraction [1], underground CO₂ sequestration [2], design of cellular solids [3], and density variations in powder processing [4]. Compaction bands, salient features of such media that develop perpendicular to major principal stress during compaction, represent zones of localized deformation where significant volume reductions occur due to grain crushing and pore collapse [5–9].

Compaction localization has been studied extensively, both experimentally and numerically. Previous works have focused predominantly on the generation of localization due to boundary stresses [10,11] and on the microstructural aspects necessary to induce localization [12–14]. In confined uniaxial compression, additional studies have revealed unique localization patterns in monotonically loaded brittle porous media, such as erratic short-lived compaction, diffused irreversible densification, and oscillatory propagation of localized compaction [15–18].

Despite the well-documented influence of boundaries on shear strain localization mechanisms in rock [19], metallic glasses [20], and granular solids [21,22], limited research has explored the effects of boundary geometry on compaction

band emergence in brittle porous media. In particular, there is no knowledge of the role of boundary geometry on the characteristics of the aforementioned oscillatory compaction band. Such conditions of combined dynamic loading and shaped boundaries are particularly relevant to powder compaction processes [23], geophysics where rock formations may contain heterogeneous inclusions [24], and compaction shock waves [25].

In this paper, we seek to assess the impact of boundary geometry on the initiation and propagation of oscillatory compaction bands in brittle porous media. To this end, we perform experiments on five different geometric configurations and demonstrate that a simple elastic model is able to capture the main effects of boundary conditions. Although this experimental study cannot encompass the variety of unique boundary conditions possible, it provides new light on the impact of non-trivial boundary effects on compaction band initiation and propagation.

II. METHODS

We use dry, brittle, oblong, puffed rice cereal (Kellogg's brand) as the test material. The test material initially has ellipsoidal grains with a mean major axis diameter of 11.27 ± 1.5 mm (one standard deviation), a mean middle axis diameter of 5.95 ± 0.64 mm, and a minor axis diameter of 3.94 ± 0.72 mm. However, these dimensions change rapidly during compression due to crushing. For each experiment, the material is placed inside a compression cell with transparent acrylic walls to minimise sidewall friction and allow video recording. Figure 1(a) shows an example of one of the experimental configurations with an initial height $H_0 = 300$ mm, a width of 150 mm, and a thickness of 50 mm. The width

Published by the American Physical Society under the terms of the Creative Commons Attribution 4.0 International license. Further distribution of this work must maintain attribution to the author(s) and the published article's title, journal citation, and DOI.

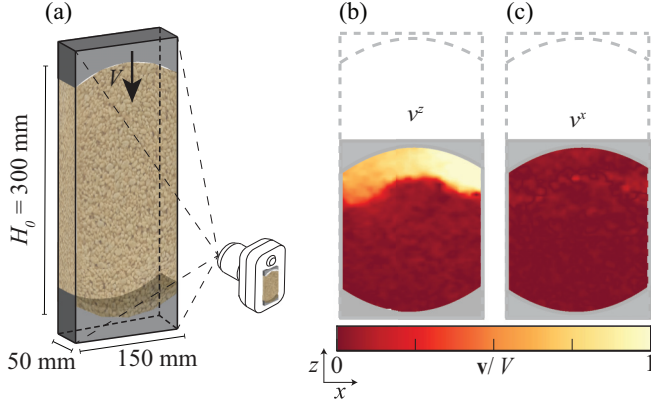


FIG. 1. Experimental methodology. (a) A representative experimental setup with curved boundaries. (b) Vertical and (c) horizontal normalized velocity field \mathbf{v}/V .

and the thickness were kept constant for all experimental configurations, and the height was typically 300 mm with some variation to allow for different boundary shapes. These dimensions are consistent with previous studies wherein compaction bands propagated in this material [15]. The material is compressed vertically at a constant velocity, $V = 1.27 \text{ mm s}^{-1}$, until a global axial strain $\varepsilon^a = \Delta H/H_0 \approx 0.45$ is achieved, where ΔH is the change in sample height from the start of the test. The axial stress versus strain demonstrated stress drops that occurred once the compaction band reached the loading piston. No discernible differences were observed between the experiments performed within this paper and previously published results, which the interested reader may find within [15,18]. The gathered video images have a resolution of $1080 \times 1920 \text{ px}$ and are sampled to 5 frames per second with PIVLAB [26] for Digital Image Correlation (DIC) analysis. This ensures that the material is displaced by approximately 1 to 2 pixels per frame, optimising accuracy. The material's velocity field is then determined as shown in Figs. 1(b)–1(c). The strain rate tensor $\dot{\boldsymbol{\varepsilon}} = \frac{1}{2}(\nabla \mathbf{v} + (\nabla \mathbf{v})^T)$ is then calculated using first-order spatial central finite differentiation. Note that we only extract planar strains from one side of the cell, not the full three-dimensional (3D) strain tensor, and assume that material behavior is independent of depth in the thickness direction. The volumetric strain $\varepsilon^v = \text{tr}(\dot{\boldsymbol{\varepsilon}})$ is determined from the trace of the strain rate tensor field, with compression taken as positive. This is used to identify the regions of localised compaction and compaction bands [7,15], characterized by high ε^v , to monitor their evolution and geometric characteristics over time.

We determine the compaction band's position at the pixel scale by assuming that such position corresponds to the global maximization of ε^v across the materials' width; this corresponds to a nondecreasing paths problem [27]. There are some localization locating methods, such as acoustic emissions [28] or manual selection [7], that can identify localisation regions but these lack the resolution necessary for determining evolving geometric characteristics. Therefore, the location and shape of the band are determined with a maximum-weighted path algorithm. Importantly, this algorithm constrains the local slope of the compaction band to a maximum of 45° (side

and corner adjacent pixels). The algorithm first generates a weight matrix $W_{i,j}$, with $i \in \{0, N\}$; $j \in \{0, M\}$ referring to indices of data points of the $N \times M$ field of ε^v . The algorithm for determining the weight matrix is

$$W_{i,0} = \varepsilon_{i,0}^v, \quad \forall i \in \{0, N\},$$

$$W_{i,j} = \max_{k \in \{-1,0,1\}} (W_{i+k,j-1}) + \varepsilon_{i,j}^v, \quad (1)$$

where, for the equation, $i \in \{1, N-1\}$ and $j \in \{1, M\}$. For $i = 0$ or $i = N$, the range of k is adjusted to $k \in \{0, 1\}$ and $k \in \{-1, 0\}$, respectively. Following the generation of the W matrix, the maximum-weighted path vector is determined by

$$\hat{z}_0 = \lambda \mathcal{I}(\max(W_{i,M})), \quad \forall i \in \{0, N\},$$

$$\hat{z}_m = \lambda \mathcal{I}(\max_{k \in \{-1,0,1\}} (W_{\hat{z}_{m-1}/\lambda+k, M-m})), \quad (2)$$

where $m \in \{1, M\}$ and \mathcal{I} is an operation that returns the index of the row for a given matrix, λ is a conversion factor in m/px , and \hat{z} is the position of the compaction band. Additionally, if $\hat{z}_m = 0$ or λN , then k must be changed accordingly, as explained for $W_{i,j}$. Note that we only take the maxima on adjacent data points (side and corners) corresponding to $k \in \{-1, 0, 1\}$ instead of on the entire height of the sample, as this could result in random and sporadic jumps in the compaction band's position due to noise in the DIC calculation and random areas of intense deformation. Further detail of this algorithm is given in the Supplemental Material (SM) [29].

III. RESULTS

For each experimental configuration, Fig. 2 displays snapshots of the ε^v field approximately two seconds apart, the location of the compaction band as determined by the algorithm above, and its direction of propagation. The configuration in Fig. 2(a), referred to as the base configuration, is used both as a reference to previous studies and for comparing the geometrical characteristics of compaction in more complex boundaries. Figures 2(b) and 2(c) show modified configurations with concave boundaries and a sloped bottom boundary, respectively. We also modified the base configuration by placing either a block at the bottom of the porous medium or a free cylinder in the center of it, as shown in Figs. 2(d) and 2(e). It is evident that a compaction band forms and propagates cyclically in all the configurations, which is consistent with previous publications [15,18]. Note that in all geometries, the band does propagate from one end of the assembly to the other in a cyclic manner, yet the direction of propagation is not universal.

Importantly, the geometry of the compaction band is clearly influenced by the vicinity of non-flat boundaries. Such variations are strikingly evident in Figs. 2(b)–2(e), which show the compaction band structure strongly influenced by the nearby boundary. For example, Figs. 2(b) and 2(c) show that the band curves or slopes nearby the non-planar boundaries. Far from any boundary, however, the band typically orients nearly horizontally. Interestingly, Fig. 2(e) shows the compaction region splits into two distinct bands before merging into a singular band at some point above the rectangular

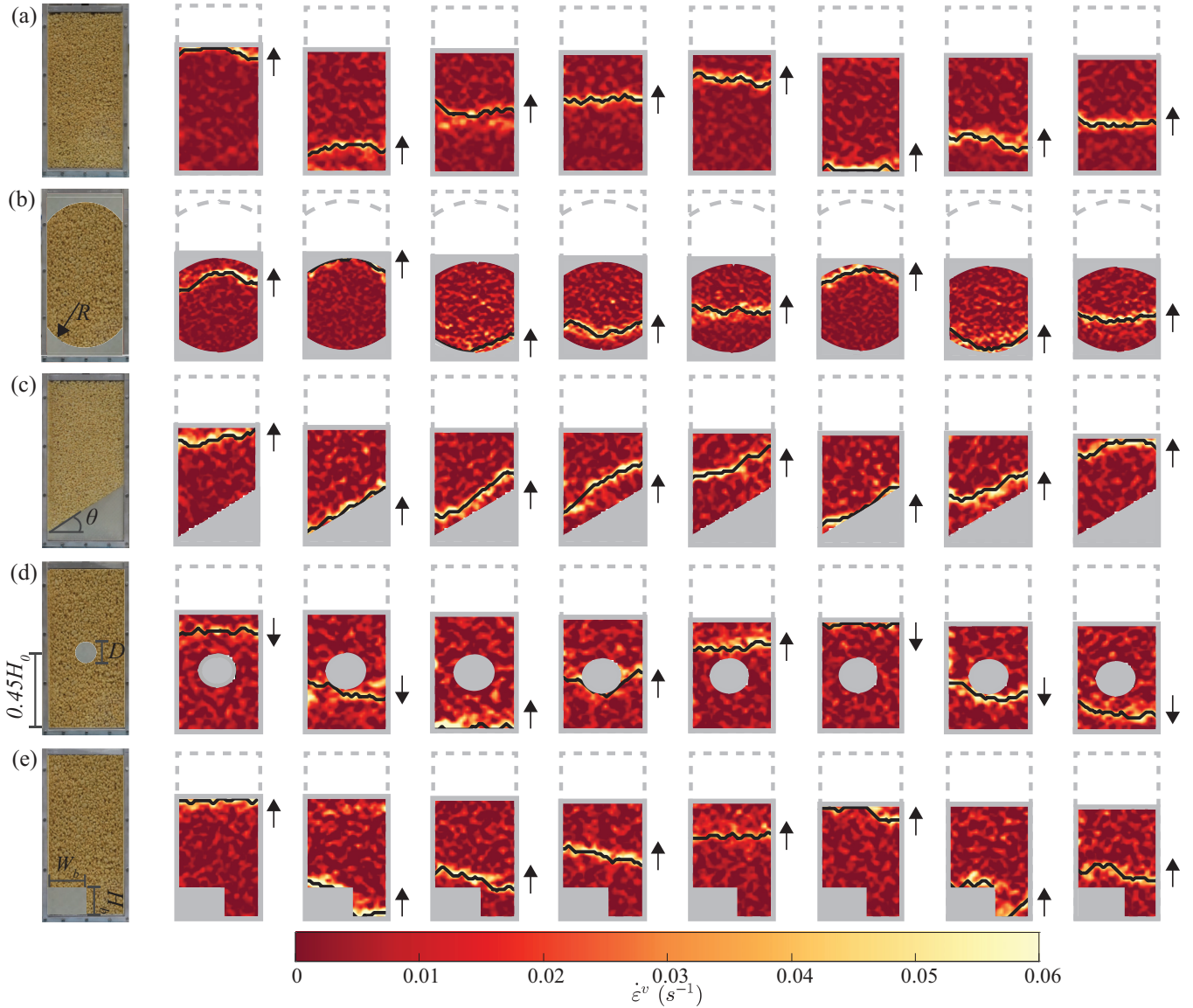


FIG. 2. Experimental geometries (first column) and corresponding volumetric strain rate $\dot{\epsilon}^v$ fields over time during a compaction band propagation. (a) Cuboidal (base) configuration, (b) concave boundary with radius $R = 90$ mm, (c) slanted bottom boundary with angle $\theta = 30^\circ$, (d) free-floating cylinder with a diameter $D = 0.4$ mm, (e) embedded rectangle with width $W_b = 75$ mm and height $H_b = 50$ mm. Each snapshot of $\dot{\epsilon}^v$ is separated by roughly 2 s. The black lines overlaying the color field denote the identified location of the compaction band, and the black arrows denote the traveling direction of the compaction band.

inclusion. Note that this observed behavior required some slight modification to the maximum-weighted path algorithm to be captured accurately as the compaction band is discontinuous, as described in detail in the SM [29]. As the band is discontinuous in that case, in the rest of the paper we will focus on the cases of Figs. 2(a)–2(d) where a single band spans the width of the apparatus.

We chose to formally characterize the geometrical characteristics of the compaction bands by representing their shape with simple functions that match the configurations shown in Figs. 2(a)–2(d). Specifically, the functions

$$z(x) = c, \quad (3a)$$

$$z(x) = \alpha x^2 + c, \quad (3b)$$

$$z(x) = \beta x + c, \quad (3c)$$

$$z(x) = \gamma(1 - x^2)^2 + c, \quad (3d)$$

were used to approximate the band shape for the experiments with planar, concave, sloped, and embedded cylinder boundaries, respectively. Note that in each function, c is related to the mean position of the compaction band, and $x \in [-1, 1]$ is the normalized x position. Thus, the band's geometry is described only by the coefficients α , β , or γ for each of the non-base configurations, and we define its location at any given time as $\bar{z} = \frac{1}{M} \sum_{i=0}^M z(x_i)$. The geometric coefficients, i.e., α , β , and γ , and c are determined by minimization of the root mean square error $R_q = \sqrt{\frac{1}{M} \sum_{i=0}^M (\hat{z}_i - z(x_i))^2}$, which is also a measure of roughness [30].

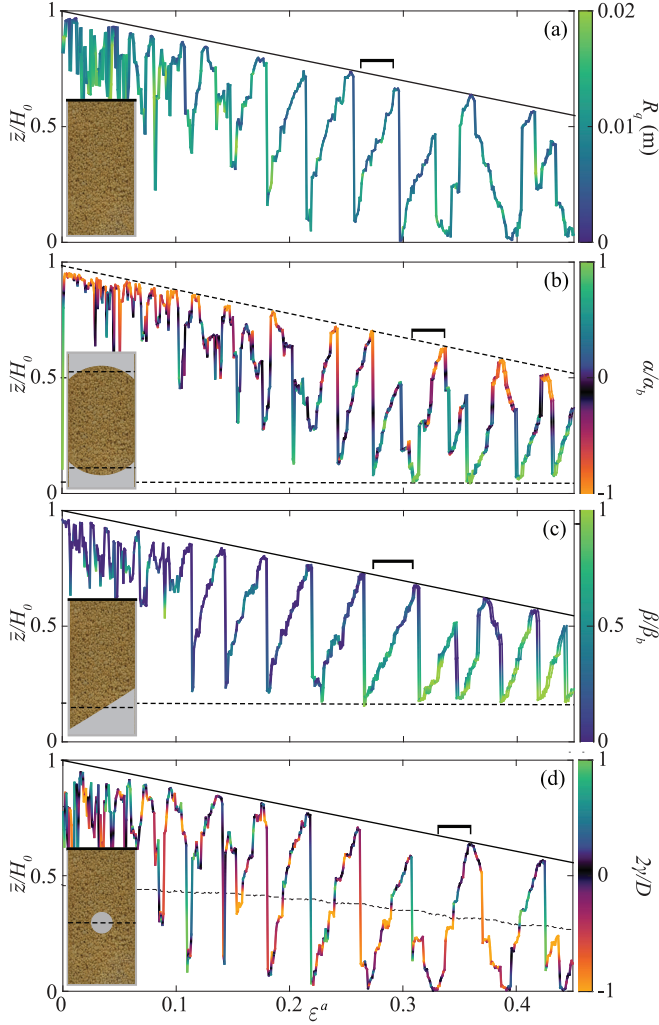


FIG. 3. Normalized compaction band position \bar{z}/H_0 plotted against axial strain ε^a . Roughness R_q and normalized geometric coefficients α/α_b , β/β_b , and $2\gamma/D$ are plotted on the color scale for the (a) base configuration, as well as for those with (b) concave, (c) sloped, and (d) embedded cylinder boundaries, respectively. Flat boundaries are displayed with solid black lines, whereas the average position of non-flat boundaries is plotted with dashed black lines. Square brackets denote the corresponding propagation cycles analyzed in Figs. 4 and 5.

Figure 3 shows the location of the compaction bands \bar{z} as the sample is compressed for the four configurations selected. The respective color scales denote the geometric characteristic of the band at a given strain. Specifically, for the base configuration, R_q is used, whereas for the concave and sloped boundaries, we indicate the normalized geometric coefficients α/α_b and β/β_b , with $\alpha_b = 0.0267 \text{ m}^{-1}$ and $\beta_b \approx 0.59$ for an ideal band that matches the boundary shape. For the embedded cylinder, the color scale displays the normalised coefficient $2\gamma/D$.

The band position and geometric shape fluctuate rapidly during the initial stages in all experiments ($\varepsilon^a \lesssim 0.15$). Oscillatory compaction is not yet established during this stage, as the deformation is pronounced near the piston and limited to the upper half of each assembly. Following this stage, i.e.,

($0.15 \lesssim \varepsilon^a \leq 0.45$), the band position for the base configuration features a coherent pattern associated with the periodic oscillation of the compaction band, between the upper and lower boundaries, which is consistent across all the tested experimental configurations. However, the concave and embedded cylinder boundaries [Figs. 3(b) and 3(c)] exhibit a less coherent pattern, and in some instances, the band fails to reach the top boundary, e.g., when $\varepsilon^a \approx 0.3$ for the concave boundary configuration. The sloped boundary [Fig. 3(c)] displays a smoother band propagation. This suggests that the concave boundary and the embedded cylinder alter the imposed stress field sufficiently to disrupt the coherency of the propagation.

Despite the observed variabilities in propagation features, the compaction band geometry exhibits unique characteristics irrespective of the configuration. In the concave boundary case, geometric coefficient variations (color scale) show that the band is primarily horizontal away from the boundaries ($|\alpha/\alpha_b| \sim 0$), but it mimics the surface shape as it approaches the boundary ($|\alpha/\alpha_b| \sim 1$). Similar geometric trends are observed in Fig. 3(c), with $\beta/\beta_b \sim 1$ near the sloped boundary. Notably, the propagating band maintains a slope while propagating for $\varepsilon^a > 0.3$. In the embedded cylinder case, the band is mostly horizontal when far from the cylinder ($|2\gamma/D| \sim 0$), but becomes temporarily pinned to the cylinder surface as it approaches and while the side portions of the band continue to propagate. This results in the abrupt change of $2\gamma/D$ from ~ -1 to $\sim +1$ when the band crosses the cylinder location.

IV. DISCUSSION

The orientation of a localization band can be determined from instability conditions [31] but requires the implementation of a rather complex constitutive model capable of exhibiting bifurcation. Here, we bypass the use for such a model by assuming that the compaction band occurs normal to the major principal stress, as observed in other works [8,9]. Thus, we opt for the simplest possible model, linear elasticity, to obtain estimations of the principal stress directions. Clearly, this implies a gross oversimplification of the material, given that puffed rice undergoes localization induced by breakage, pore collapse, and plastic rearrangements, and thus exhibits a nonlinear, serrated stress-strain response [32]. However, linear elasticity provides a reasonable field of stress distribution within the material, with the advantage of simplicity.

We performed a quasi-static generalized plane-strain boundary value problem with the Finite Element Method (FEM) software MOOSE [33]. To achieve this, we simulated material compression for the strain segments denoted by the square brackets in Fig. 3. We utilized homogeneous isotropic linear elasticity and modelled the interaction between the internal media and the boundaries with a frictionless penalty contact. The bulk modulus $K = 0.1 \text{ MPa}$ was used with a Poisson's ratio $\nu = 0.2$. Note that the choice of K does not influence the principal stress directions. However, ν does, as it was found that as ν increases there is a more pronounced curvature near shaped boundaries. For Poisson's ratio, we assume $\nu = 0.20$, which is within the range of typical values for open porous foams [34] and rocks [35], since the Poisson's ratio of the material is unknown. The confining cell

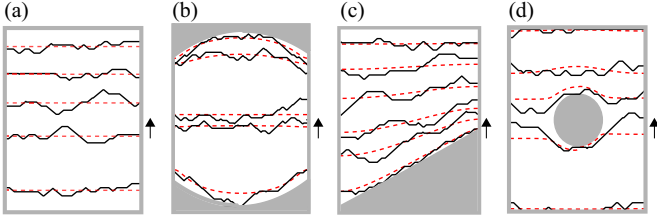


FIG. 4. Comparison of FEM characteristic lines of minor principal stress (dashed red line) and compaction band location (solid black line) for (a) base configuration, (b) concave boundaries, (c) sloped boundary, and (d) embedded cylinder. Note that compaction band positions are snapshots, with the band's first position occurring at the bottom of the experimental configuration and the arrows indicating the direction of the band's propagation.

material properties were $K = 1$ MPa and $\nu = 0.3$ to ensure the exterior material was sufficiently rigid. Furthermore, the internal boundaries of the compression cell are restrained from movement, and thus, ν for the compression cell does not play a role in the interaction behavior. The contact penalty parameters were selected to ensure less than 0.002 m of interpenetration.

The characteristic lines of principal stress were determined by first calculating the principal stress directions at each node and then interpolating these values to estimate the minor principal stress direction at specific points. We start at one boundary and incrementally used the calculated directions to compute the next coordinate along the characteristic line, repeating until the opposite boundary is reached.

Figure 4 shows snapshots of the location of the compaction band at a few discrete times, compared with the characteristic lines that fit them best from the simulations. The best-fit characteristic lines were determined by minimising the mean square residual, as previously done with Eqs. (3a) to (3d). As expected, in the base configuration used in Fig. 4(a), the minor principal stress characteristics can be matched closely with the essentially horizontal bands, albeit with some deviation that emerges naturally due to material heterogeneity, as observed in the field [36] and other numerical simulations [5].

More surprisingly though, the characteristic lines capture the band's geometric change in the vicinity of the concave and sloped boundaries remarkably well, as shown in Figs. 4(b) and 4(c), respectively. Moreover, for the sloped boundary case, the slope of the characteristic lines reduces with height, similar to the compaction band. Similarly, Fig. 5(b) shows that the characteristic lines curve around the embedded circle. Yet, these results are primarily qualitative in nature. In Fig. 5(a), the values of R_q are plotted for all experimental configurations, where we now use the height of the best fit characteristic line $z_e(x_i)$ for determination of the band's roughness instead of the model heights given by Eqs. (3a) to (3d). Notably, all experiments produce bands with the same roughness with respect to the characteristic lines, suggesting that they are a good model for the band locations. Figure 5(b) shows the differential roughness $\delta R_q = R_q - R_q^f$, where R_q^f represents the roughness under the assumption of a horizontal band for the concave,

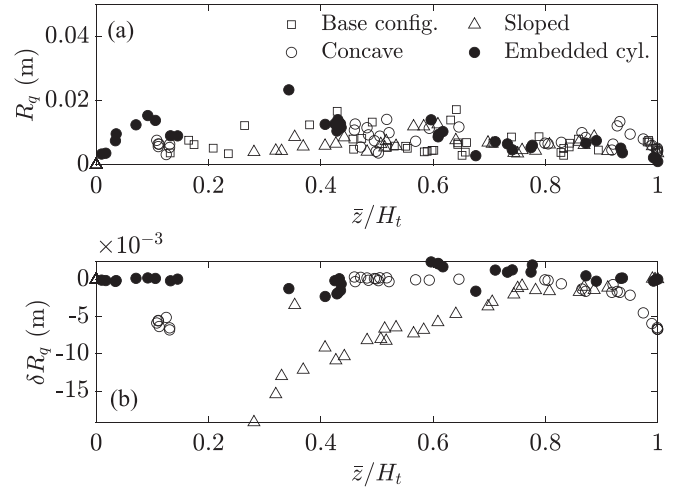


FIG. 5. Analysis of fit of characteristic lines of minor principle stress for a single propagation cycle. (a) Roughness R_q against the normalised height of compaction band \bar{z}/H_t , where H_t is the maximum height at the end of the propagation cycle shown by the black bracket in Fig. 3. (b) Differential roughness $\delta R_q = R_q - R_q^f$ against normalized height, where R_q^f is the roughness assuming a horizontal minor principle stress.

sloped, and embedded cylinder boundaries as opposed to resulting minor principal stress characteristics. It becomes evident that for both the concave and sloped boundaries, near the boundary, $\delta R_q < 0$, which indicates that the compaction band geometry is generally better approximated through the principal stress rotations induced by the shaped boundary. However, farther from the boundary, $\delta R_q \approx 0$, which implies that the band reverts to a nearly horizontal orientation, as demonstrated by the qualitative comparison in Fig. 4 and the quantitative depiction of band shape in Fig. 3. Additionally, δR_q offers insights into how far from the boundary the shape of the compaction band remains unaffected. It is worth noting that the sloped boundary appears to transition progressively to horizontal, without a discernible critical distance, a trait not evident for the embedded cylinder case. To a lesser degree, the concave boundary shows this transition as well, but this transition occurs over a much shorter distance. The results found indicate that to first order, simple linear elasticity can be used to predict principal plane orientations, which are in turn linked to compaction band orientations. Of course, a more advanced constitutive law for the material should be able to provide a more accurate description of the compaction instability and, in particular, give information on band propagation that is inaccessible to the linear elastic equilibrium simulations.

V. CONCLUSION

In conclusion, using compression experiments on puffed rice assemblies, we reveal that boundary shapes substantially affect the initiation and propagation of oscillatory compaction bands in brittle porous media. Compaction bands are generated even at curved or inclined boundaries and propagate persistently despite encountering an obstacle. In addition to this consistent propagation, we found that the shape of a compaction band assumes the shape of

the boundary it approaches. A linear elastic analysis suggests that the characteristic lines of minor principal stress provide a first-order approximation of the shape of the band. While this model offers insight into the compaction band's shape, advanced constitutive laws, such as those in [32], are essential for understanding band propagation dynamics and the influence of complex boundaries. Such models would involve recurrent softening linked to potential instabilities necessitating advanced numerical schemes, which are currently under study. Our study provides valuable insight into the roles that boundary conditions play on strain localisa-

tion mechanisms, which are in turn significant for the analysis of relevant natural processes and for the design of engineering materials and operations.

ACKNOWLEDGMENTS

The authors would like to thank the Australian Research Council for funding through DP190103487 and the San Diego State University Research Foundation (260795). The authors also wish to thank Yanni Chen and Leonardo Crespo-Parraga for the fruitful discussions.

-
- [1] M. Hettema, E. Papamichos, and P. Schutjens, Subsidence delay: Field observations and analysis, *Oil Gas Sci. Technol.* **57**, 443 (2002).
- [2] L. Räss, R. Y. Makhnenko, Y. Podladchikov, and L. Laloui, Quantification of viscous creep influence on storage capacity of Caprock, *Energy Procedia* **114**, 3237 (2017).
- [3] S. D. Papka and S. Kyriakides, In-plane crushing of a polycarbonate honeycomb, *Int. J. Solids Struct.* **35**, 239 (1998).
- [4] O. Simon and P. Guigon, Correlation between powder-packing properties and roll press compact heterogeneity, *Powder Technol.* **130**, 257 (2003).
- [5] L. Blatny, P. Berclaz, F. Guillard, I. Einav, and J. Gaume, Microstructural origin of propagating compaction patterns in porous media, *Phys. Rev. Lett.* **128**, 228002 (2022).
- [6] A. Das, G. D. Nguyen, and I. Einav, Compaction bands due to grain crushing in porous rocks: A theoretical approach based on breakage mechanics, *J. Geophys. Res.: Solid Earth* **116**, D00P06 (2011).
- [7] Y. Abdallah, J. Sulem, M. Bornert, S. Ghabezloo, and I. Stefanou, Compaction banding in high-porosity carbonate rocks: 1. Experimental observations, *J. Geophys. Res.: Solid Earth* **126**, e2020JB020538 (2021).
- [8] D. Holcomb, J. W. Rudnicki, K. A. Issen, and K. Sternlof, Compaction localization in the earth and the laboratory: State of the research and research directions, *Acta Geotech.* **2**, 1 (2007).
- [9] T.-f. Wong and P. Baud, The brittle-ductile transition in porous rock: A review, *J. Struct. Geol.* **44**, 25 (2012).
- [10] E. Klein, P. Baud, T. Reuschlé, and T. Wong, Mechanical behaviour and failure mode of bentheim sandstone under triaxial compression, *Physics and Chemistry of the Earth, Part A: Solid Earth and Geodesy* **26**, 21 (2001).
- [11] S. Tembe, P. Baud, and T.-f. Wong, Stress conditions for the propagation of discrete compaction bands in porous sandstone, *J. Geophys. Res.: Solid Earth* **113**, 2007JB005439 (2008).
- [12] C. S. Cheung, P. Baud, and T.-f. Wong, Effect of grain size distribution on the development of compaction localization in porous sandstone, *Geophys. Res. Lett.* **39**, 2012GL053739 (2012).
- [13] A. Rustichelli, E. Tondi, F. Agosta, A. Cilona, and M. Giorgioni, Development and distribution of bed-parallel compaction bands and pressure solution seams in carbonates (Bolognano formation, Majella mountain, Italy), *J. Struct. Geol.* **37**, 181 (2012).
- [14] H. Wu, J. Zhao, and W. Liang, The signature of deformation bands in porous sandstones, *Rock Mech. Rock Eng.* **53**, 3133 (2020).
- [15] J. R. Valdes, F. L. Fernandes, and I. Einav, Periodic propagation of localized compaction in a brittle granular material, *Granular Matter* **14**, 71 (2012).
- [16] F. Guillard, P. Golshan, L. Shen, J. R. Valdes, and I. Einav, Dynamic patterns of compaction in brittle porous media, *Nat. Phys.* **11**, 835 (2015).
- [17] T. W. Barraclough, J. R. Blackford, S. Liebenstein, S. Sandfeld, T. J. Stratford, G. Weinländer, and M. Zaiser, Propagating compaction bands in confined compression of snow, *Nat. Phys.* **13**, 272 (2017).
- [18] J. R. Valdes, F. Guillard, and I. Einav, Evidence that strain-rate softening is not necessary for material instability patterns, *Phys. Rev. Lett.* **119**, 118004 (2017).
- [19] G. Shahin and G. Buscarera, Simulation of emergent compaction banding fronts caused by frictional boundaries, *Geotech. Lett.* **10**, 436 (2020).
- [20] W. Li, Y. Gao, and H. Bei, Instability analysis and free volume simulations of shear band directions and arrangements in notched metallic glasses, *Sci. Rep.* **6**, 34878 (2016).
- [21] D. Shuttle and I. Smith, Numerical simulation of shear band formation in soils, *Int. J. Numer. Anal. Methods Geomech.* **12**, 611 (1988).
- [22] Z. Gao and J. Zhao, Strain localization and fabric evolution in sand, *Int. J. Solids Struct.* **50**, 3634 (2013).
- [23] M. S. Kadiri and A. Michrafy, The effect of punch's shape on die compaction of pharmaceutical powders, *Powder Technol.* **239**, 467 (2013).
- [24] A. Nicol, C. Childs, J. Walsh, and K. Schafer, A geometric model for the formation of deformation band clusters, *J. Struct. Geol.* **55**, 21 (2013).
- [25] A. Mandal and K. Gonthier, Thermomechanics of transient oblique compaction shock reflection from a rigid boundary, *Shock Waves* **25**, 589 (2015).
- [26] W. Thielicke and R. Sonntag, Particle image velocimetry for Matlab: Accuracy and enhanced algorithms in PIVLAB, *J. Open Res. Softw.* **9**, 12 (2021).
- [27] V. V. Williams, Nondecreasing paths in a weighted graph or: How to optimally read a train schedule, *ACM Transactions on Algorithms (TALG)* **6**, 1 (2010).
- [28] J. Fortin, S. Stanchits, G. Dresen, and Y. Guéguen, Acoustic emission and velocities associated with the formation of compaction bands in sandstone, *J. Geophys. Res. Solid Earth* **111** (2006).
- [29] See Supplemental Material at <http://link.aps.org/supplemental/10.1103/PhysRevE.108.064906> for description of the maximum weighted path algorithm.

- [30] American Society of Mechanical Engineers, *Surface Texture (Surface Roughness, Waviness, and Lay)*, ASME B46.1-2009 (ASME, New York, 2010).
- [31] J. W. Rudnicki and J. Rice, Conditions for the localization of deformation in pressure-sensitive dilatant materials, *J. Mech. Phys. Solids* **23**, 371 (1975).
- [32] D. Riley, I. Einav, and F. Guillard, A constitutive model for porous media with recurring stress drops: From snow to foams and cereals, *Int. J. Solids Struct.* **262–263**, 112044 (2023).
- [33] A. D. Lindsay, D. R. Gaston, C. J. Permann, J. M. Miller, D. Andrš, A. E. Slaughter, F. Kong, J. Hansel, R. W. Carlsen, C. Icenhour, L. Harbour, G. L. Giudicelli, R. H. Stogner, P. German, J. Badger, S. Biswas, L. Chapuis, C. Green, J. Hales, T. Hu *et al.*, 2.0 - MOOSE: Enabling massively parallel multiphysics simulation, *SoftwareX* **20**, 101202 (2022).
- [34] L. J. Gibson and M. F. Ashby, *Cellular Solids: Structure and Properties*, Cambridge Solid State Science Series, 2nd ed. (Cambridge University Press, Cambridge, 1997).
- [35] H. Gercek, Poisson's ratio values for rocks, *Int. J. Rock Mech. Min. Sci.* **44**, 1 (2007).
- [36] C. Liu, D. D. Pollard, S. Deng, and A. Aydin, Mechanism of formation of wiggly compaction bands in porous sandstone: 1. Observations and conceptual model, *J. Geophys. Res.: Solid Earth* **120**, 8138 (2015).